Materials Chemistry and Physics 355 (2026) 132238

Contents lists available at ScienceDirect

Materials Chemistry and Physics

journal homepage: www.elsevier.com/locate/matchemphys

Selective gas sensing and electronic response of Al-decorated phographene (Al-*d*-PHOG) nanosheets: Insights from DFT and electron density analyses

Bhishma Karki [a,l,*], Ahmed Aldulaimi [b], Omayma Salim Waleed [c], G. PadmaPriya [d], Subhashree Ray [e], Y. Sasikumar [f], Renu Sharma [g], Shakhbozjon Tursunboev [h], Fazliddin Jalilov [i], Mutabar Latipova [j,m], Aseel Smerat [k]

[a] *Department of Physics, Tri-Chandra Multiple Campus, Tribhuvan University, Kathmandu, 44600, Nepal*
[b] *Department of Pharmacy, Al-Zahrawi University, Karbala, Iraq*
[c] *Department of Anesthesia Techniques, Health and Medical Techniques College, Alnoor University, Mosul, Iraq*
[d] *Department of Chemistry and Biochemistry, School of Sciences, JAIN (Deemed to be University), Bangalore, Karnataka, India*
[e] *Department of Biochemistry IMS and SUM Hospital, Siksha 'O' Anusandhan, Bhubaneswar, Odisha, 751003, India*
[f] *Department of Chemistry, Sathyabama Institute of Science and Technology, Chennai, Tamil Nadu, India*
[g] *Department of Chemistry, University Institute of Sciences, Chandigarh University, Mohali, Punjab, India*
[h] *Kimyo International University in Tashkent, Shota Rustaveli str. 156, Tashkent, 100121, Uzbekistan*
[i] *Department of Pharmaceutical and Chemistry, Alfraganus University, Tashkent, 100190, Uzbekistan*
[j] *National Research University TIIAME, Kori Niyoziy 39, Tashkent, 100000, Uzbekistan*
[k] *Hourani Center for Applied Scientific Research, Al-Ahliyya Amman University, Amman 19328, Jordan*
[l] *National Research Council Nepal, New Baneshwor-10, Kathmandu, ↱↱44600, Nepal*
[m] *University of Tashkent for Applied Sciences, Str. Gavhar 1, Tashkent 100149, Uzbekistan*

HIGHLIGHTS

- Aluminum-decorated phographene (Al-*d*-PHOG) exhibits selective gas adsorption.
- NH_3 and NO_2 induce partial chemisorption, while CO and CO_2 remain physisorbed.
- Recovery kinetics, charge transfer, and electronic structure shifts establish Al-*d*-PHOG as a high-response, nanosensor.
- The study provides a predictive framework connecting adsorbate electronic properties to nanosheet response.

GRAPHICAL ABSTRACT

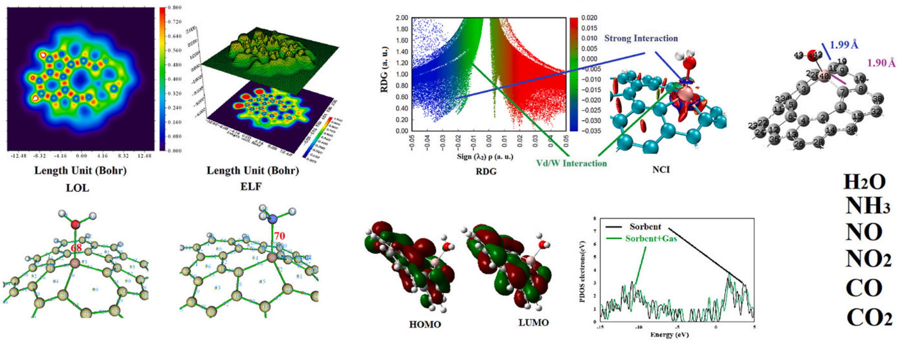

ARTICLE INFO

Keywords:
Al-dopped phographene (Al-*d*-PHOG)
Sensor
Hazardous gases

ABSTRACT

This study presents a comprehensive theoretical investigation of gas adsorption on aluminum-decorated Phographene (Al-*d*-PHOG) nanosheets, focusing on CO, CO_2, H_2O, NH_3, NO, and NO_2. Using DFT with B3LYP-D3/6-311G(d,p), optimized geometries, adsorption energies, charge transfer, and frontier molecular orbitals were analyzed alongside PDOS, RDG–NCI, ELF/LOL, and bond critical point evaluations. Results reveal a pronounced

---

* Corresponding author.
E-mail address: bhishma.karki@trc.tu.edu.np (B. Karki).

https://doi.org/10.1016/j.matchemphys.2026.132238
Received 9 December 2025; Received in revised form 31 January 2026; Accepted 15 February 2026
Available online 20 February 2026

Sorbent
Weak interaction studies

selectivity: NH_3 and NO_2 induce strong electronic perturbations, localized orbital redistribution, and partial chemisorptive interactions at Al sites, while H_2O exhibits moderate effects, and CO, CO_2, and NO remain largely physisorbed. Recovery times and structural changes further corroborate these distinctions, highlighting kinetic and operational constraints for sensing applications. The study elucidates the mechanistic link between electron density redistribution and sensor response, providing a predictive framework for adsorbate selection. These insights demonstrate Al-*d*-PHOG as a selective, high-response nanosensor platform, emphasizing the importance of electronic compatibility for designing efficient and reversible gas detection systems.

1. Introduction

Global atmospheric pollution has escalated into a pressing concern for human health, environmental regulation, and scientific inquiry alike [1]. This growing problem stems from the persistent emission of particulate matter and reactive gases into the troposphere, originating from natural phenomena but driven predominantly by human industrial and urban activities [2]. Major contributors to air degradation include nitrogen-based oxidants [3], sulfurous pollutants [4], and carbon-centered gaseous species [5], most of which are closely tied to anthropogenic output [6]. Extensive studies now demonstrate that these contaminants regardless of their specific origin significantly heighten carcinogenic risks [7] and exacerbate chronic or acute respiratory disorders [8]. Such findings underscore the immediate necessity of minimizing human exposure to polluted air masses [9]. Consequently, technologies capable of detecting, capturing, or breaking down hazardous airborne species particularly through adsorption or catalytic pathways have become a focal point of contemporary research efforts [10–13].

Nowadays, nanomaterials play a vital role and have numerous applications in the fields of biotechnology, electronic, water treatment, environmental pollution detection and control, food industries, catalyst, medicine, and so on [14–17]. The accelerated advancement of nanotechnology has further strengthened the scientific pursuit of high-performance materials capable of addressing the environmental challenges, as evidenced by a wide array of recent investigations [18–20]. Because of their unique structural and electronic characteristics, numerous nanomaterials have been designed to sense, immobilize, or neutralize toxic species [21–24]. This progress has stimulated the creation of increasingly sophisticated nanostructures, especially those tailored through heteroatom incorporation or other targeted modifications [25–27]. Common design routes include substitutional doping, surface functionalization, and deliberate manipulation of nanoscale dimensions and morphology [28–30].

Computational approaches particularly Density Functional Theory have become essential for predicting and rationalizing the behavior of pristine and engineered nanomaterials, ranging from atomic clusters [31–33] and fullerene-like species [34–36] to emerging two-dimensional architectures [37–39]. A substantial body of quantum-chemical evidence confirms that these methods reliably characterize structural stability, electronic response, and adsorption behavior across diverse material platforms [40,41]. Within this scientific landscape, PHOG-based nanosheets have recently attracted notable interest due to their unusual bonding framework and favorable electronic attributes [42,43]. Aluminum was selected as the decorating atom due to its low atomic mass, high abundance, low toxicity, and strong interaction with polar gas molecules. Compared to many transition metals, Al induces significant electronic modulation while avoiding excessive chemisorption or magnetic complexity, which is advantageous for achieving reversible and selective gas sensing [44,45]. The stability of Al decoration is supported by the short Al–C bond length, significant charge transfer, and strong localization of electron density at the anchoring site, indicating robust binding and a low tendency for migration or clustering.

Building on this foundation, the present work investigates the adsorption characteristics of Al-*d*-PHOG toward several major atmospheric pollutants (CO_2, CO, H_2O, NH_3, NO, and NO_2) using DFT calculations complemented by critical-point analysis as well as RDG, NCI, ELF, and LOL tools to elucidate the detailed molecular mechanisms governing gas–surface interactions.

2. Computational details

To explore how Al-*d*-PHOG interacts with several major atmospheric contaminants (CO_2, CO, H_2O, NH_3, NO, and NO_2), each gas species was initially generated as an isolated molecular model and used as the starting point for independent geometry optimizations. These individual structures, together with the pristine nanosheet, were fully optimized using the B3LYP-D3 functional paired with the 6-311G(d,p) basis set, ensuring that all resulting configurations correspond to true minima on the potential energy surface. The B3LYP-D3/6-311G(d,p) method was adopted to accurately describe local electronic and noncovalent interactions governing gas adsorption on Al-*d*-PHOG. A finite cluster model was used to enable detailed real-space analyses (ELF, LOL, RDG–NCI), which are less accessible in periodic calculations. Previous studies indicate that, for localized adsorption, such cluster-based approaches reproduce the qualitative trends of periodic DFT, and therefore similar adsorption selectivity is expected [46]. Temperature effects were considered through a thermally activated desorption model used to estimate recovery times. An increase in temperature is expected to weaken adsorption strength and significantly reduce recovery times, particularly for weakly physisorbed molecules such as CO, CO_2, and NO. Under humid conditions, H_2O molecules exhibit moderate adsorption at the Al active site and may compete with target gas molecules for available binding sites, which can partially reduce sensing selectivity. This effect may be alleviated through operating temperature optimization or surface functionalization, and should be considered when evaluating sensor performance under realistic environmental conditions. After establishing the equilibrium geometries of the isolated components, adsorption complexes were assembled and subjected to the same computational treatment to obtain their relaxed structures and relevant electronic descriptors. All quantum-chemical calculations were executed within the Gaussian 16 suite [47].

The use of the B3LYP-D3/6-311G(d,p) framework provides a dependable foundation for structural and electronic accuracy, a fact supported by numerous earlier investigations employing identical or comparable methodologies [48–50]. The BSSE was accounted for from the initial calculations using the counterpoise method. To assess how electron density is redistributed during the adsorption process, the Global Electron Density Transfer (GEDT) parameter was evaluated following the standard theoretical approach [51]. This quantity offers a direct measure of the extent and direction of charge flow between the Al-*d*-PHOG-based substrate and the adsorbed gas molecule, enabling a clearer interpretation of the underlying electronic response.

$$GEDT = \Sigma q_A \tag{1}$$

Where; q_A is the atoms' net Mulliken charges of each gas. Also, the Fermi level (E_F) of each adsorption complex, was estimated by relation (2) [52]:

$$E_F = -1*(E_{LUMO} + E_{HOMO}) / 2 \tag{2}$$

Where; E_{LUMO} and E_{HOMO}, are the energy surfaces of LUMO, and HOMO, respectively. In addition, the E_g of each system was reached by formula (3) [53]:

$$E_g = (E_{LUMO}\text{-}E_{HOMO}) \tag{3}$$

Also, the adsorption energy (E_{ads}) was computed by relation 4:

$$E_{ads} = E_{sys}\text{-}(E_s + E_{gs}) \tag{4}$$

In this expression, E_{sys} denotes the total electronic energy of the optimized adsorption complex, while E_s refers to the energy of the isolated Al-*d*-PHOG nanosheet and E_{gas} represents the computed energy of the corresponding free gas molecule. To further substantiate the trends obtained from the Global Electron Density Transfer (GEDT) analysis, a Natural Bond Orbital (NBO) evaluation was carried out [54]. This complementary approach provides a detailed description of donor–acceptor interactions and charge redistribution within the system, thereby offering an independent verification of the electronic behavior inferred from GEDT.

The Global hardness

$$\eta = (I\text{-}A)/2 \tag{5}$$

Softness

$$S = 1/2\eta \tag{6}$$

In this formulation, the electron affinity *A* is defined as the negative of the LUMO energy ($-E_{LUMO}$), while the ionization potential *I* corresponds to the negative of the HOMO energy ($-E_{HOMO}$). These parameters establish the foundational electronic descriptors used for interpreting reactivity and charge-transfer tendencies within the system.

Lastly, the electrical conductivity (σ) of both the pristine nanosheet and its gas-adsorption complexes was evaluated through relation 7, enabling a direct correlation between the computed electronic-structure variations and the anticipated sensing performance of the material.

$$\sigma = AT^{-3/2}\exp(-E_g / 2K_bT) \tag{7}$$

Where, A is the Richardson's constant ($6(10^5)$ A/m^2), K_b refers the (1.380649×10^{-23} J/K) (the Boltzmann constant), Temperature is T (K), and E_g (eV) is the value of the band gap [55,56]. Also, the recovery time or the τ parameter was computed by using equation (8) [57,58]:

$$\tau = \upsilon^{-1}\exp(-E_{ads} / K_bT) \tag{8}$$

where υ^{-1} is the attempt frequency. In these calculations, an attempt frequency of $10^{12}s^{-1}$ has been considered.

The subtle noncovalent forces governing the interaction between each gas molecule and the Al-*d*-PHOG nanosheet were characterized using the non-covalent interaction (NCI) framework [59], which relies on the reduced density gradient (RDG) derived from the quantum-mechanical electron density distribution. All NCI-related analyses were conducted with Multiwfn 3.7 [60], where the RDG function was evaluated in conjunction with the second eigenvalue of the electron-density Hessian to distinguish attractive, weakly repulsive, and steric regions. The resulting color-mapped RDG scatter diagrams were generated with gnuplot 5.7, while three-dimensional RDG isosurfaces were rendered in Visual Molecular Dynamics (VMD) [61], enabling direct visualization of interaction domains around the nanosheet. To accurately account for dispersion contributions, adsorption energies (E_{ads}) were re-evaluated using the same B3LYP-D3/6-311G(d,p) computational framework [49,62,63].

To further refine the interpretation of interaction patterns, both the Electron Localization Function (ELF) and the Localized Orbital Locator (LOL) were calculated for each optimized adsorption system. These complementary descriptors illuminate the distribution and confinement of electron density, identifying regions of localized bonding, delocalized charge, and weak intermolecular stabilization. When considered together, the RDG, ELF, and LOL analyses establish a detailed and coherent understanding of how the Al-*d*-PHOG nanosheet engages electronically and structurally with the examined gas molecules, revealing the full spectrum of interaction strengths and bonding characteristics across the adsorption complexes.

3. Results and discussion

For each gas molecule, several initial adsorption configurations were considered, including different molecular orientations, approach directions, and initial distances relative to the Al site. All structures were fully optimized without constraints. The most stable configuration was identified as the global minimum based on the lowest total energy and the absence of imaginary vibrational frequencies. Each isolated system was then subjected to an exhaustive structural optimization employing the B3LYP-D3 method in combination with the 6-311G(d,p) basis set. The D3 dispersion correction was applied to account for van der Waals interactions and has been widely validated for gas adsorption on metal-decorated and low-dimensional materials. Although direct experimental data for Al-decorated phographene are not yet available, the computed adsorption energies for CO, CO_2, and NO are consistent with values reported for similar 2D systems. Comparative tests with alternative dispersion schemes, such as D3(BJ), indicate that the relative adsorption trends remain robust, supporting the reliability of the reported selectivity. This level of theory provides a practical balance between the accuracy needed to capture dispersion-driven effects and the numerical stability required for reliable convergence. The optimization procedure ensures that every final geometry corresponds to a genuine minimum on the potential energy surface, avoiding artifacts such as higher-order stationary points or partially converged structures. The Al-*d*-PHOG nanosheet was modeled with the Al atom positioned at the cluster center and all peripheral dangling bonds passivated with hydrogen atoms to minimize edge effects. PDOS, FMO, and ELF/LOL analyses confirm that adsorption-induced electronic perturbations are localized around the Al site and do not extend to the cluster boundaries, ensuring reliable evaluation of adsorption geometries and energetics. The resulting equilibrium configurations for all standalone molecules and for the pristine nanosheet are displayed in Fig. 1 and serve as the structural benchmarks for the subsequent adsorption, charge-transfer, and electronic-property evaluations. To reduce finite-size and edge effects, the Al atom was placed at the central region of the phographene cluster, while all peripheral dangling bonds were passivated with hydrogen atoms. This strategy effectively suppresses artificial edge states near the Fermi level. PDOS, FMO, and ELF/LOL analyses indicate that the electronic changes induced by gas adsorption are mainly localized around the Al site and its nearest neighbors, with negligible contribution from the cluster edges.

3.1. Geometrical analysis, absorption energies, and recovery times

For radical species (NO, NO_2), geometry optimizations were performed for multiple spin multiplicities. The reported structures correspond to the lowest-energy spin state, verified by total energy comparisons and the absence of imaginary vibrational frequencies, ensuring that the optimized configurations represent the true ground state. In the pristine Al-*d*-PHOG nanosheet (Table and Fig. 1), the intramolecular C–Al bond of 1.88 Å serves as the structural anchor controlling how the electron density around Al responds to incoming molecules. Once H_2O and NH_3 approach the surface, the framework deforms in a consistent and telling manner: the C–Al bond elongates to 1.90 Å and the newly formed Al–O/N contacts tighten to 1.99–2.05 Å, indicating a shift from mere physisorption toward partial chemisorption. Their adsorption energies, −1.22 eV for H_2O and −1.53 eV for NH_3, confirm an interaction that is far too strong to be advantageous for fast-cycle sensing. The recovery times τ $1.43(10^{10})$ s for H_2O and an extreme $2.52(10^{15})$ s for NH_3 demonstrate a near-irreversible occupation of active sites. Using the standard τ ≈ 1 relation, these τ values imply

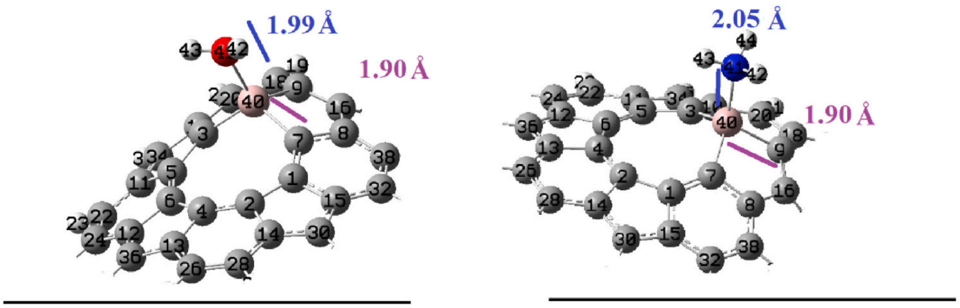

Al-d-PHOG + H2O

Al-d-PHOG + NH3

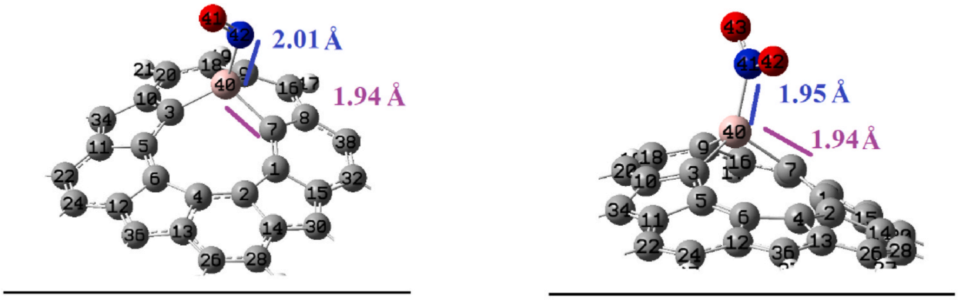

Al-d-PHOG + NO

Al-d-PHOG + NO2

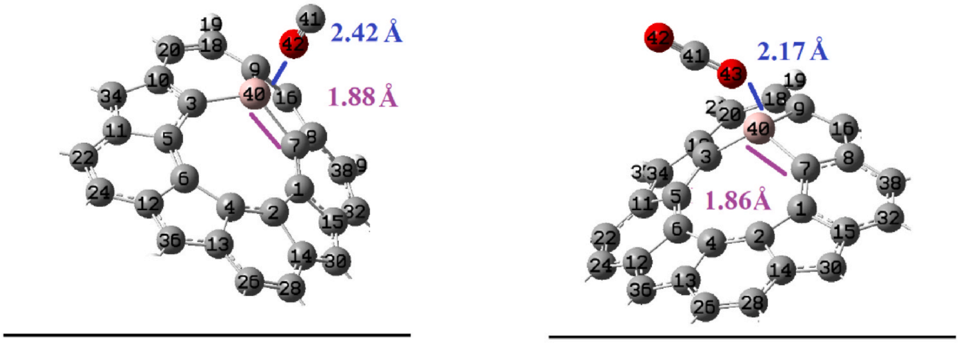

Al-d-PHOG + CO

Al-d-PHOG + CO2

Fig. 1. The optimized structures of Al-*d*-PHOG nanosheet and its adsorption systems with each gas.

extraordinarily low desorption rates, driving the surface coverage parameter θ toward unity and effectively locking the system into a saturated state. Charge transfer corroborates this: NH_3 donates noticeably (GEDT = 0.19) whereas H_2O remains neutral, yet both cause enough stabilization to make detachment kinetically prohibitive. Thus, while the optimized structures (Fig. 1) show Al engaging cleanly with each adsorbate, these two gases over-stabilize the surface in a counterproductive manner. If one seeks reversible sensing, both molecules push Al-*d*-PHOG into a dead-end operational regime.

The interactions with NO and NO_2 reveal a sharply divergent kinetic character one beneficial, one destructive. NO exhibits a mild adsorption energy (−0.26 eV) combined with a negative GEDT (−0.33), indicating electron transfer from the gas to the surface but without structural overcommitment. The Al–N distance of 2.01 Å confirms a restrained interaction. This manifests kinetically as an exceptionally fast recovery time, $\tau = 8.33(10^{-7})$ s, implying a very high desorption constant and a correspondingly low steady-state coverage θ. In other words, NO continuously binds and detaches, enabling high-frequency detection cycles. NO_2, in contrast, overwhelms the surface. Its adsorption energy of −3.52 eV is effectively in the chemisorption regime; the Al–N distance collapses to 1.95 Å and charge transfer becomes strongly negative (−0.57). The kinetic consequence is catastrophic: τ rises to $1.44(10^{49})$ s, making the desorption process essentially zero. Under any realistic model, θ tends to full site occupation. Once bound, NO_2 is practically permanent, disabling the material as a reusable sensor but marking it as a potent molecular trap. This stark contrast between NO and NO_2 exposes the limits of Al-*d*-PHOG's tunability and highlights which species exploit its active site without destroying its reversibility.

With CO and CO_2, Al-*d*-PHOG settles into a far more balanced adsorption regime neither too weak to register nor too strong to release. Their adsorption energies (−0.13 eV for CO, −0.33 eV for CO_2) reflect predominantly van der Waals stabilization. Charge transfer is modest and consistent with this interpretation (−0.14 for CO and −0.32 for CO_2), indicating limited distortion of the Al electronic environment. Structurally, the Al–O distances 2.42 Å for CO and 2.17 Å for CO_2 place these interactions well within the physisorption domain, reinforcing fast kinetics. Indeed, τ values of $5.27(10^{-9})$ s (CO) and $1.27(10^{-5})$ s (CO_2) correspond to high τ and therefore small equilibrium coverage θ. This means the nanosheet rapidly frees its active sites after each interaction, maintaining continuous sensing capability. These behaviors align cleanly with first-order kinetic models, where adsorption and desorption remain in dynamic balance without structural lock-in. Equation (8) was employed as a comparative descriptor of adsorption kinetics rather than a precise predictor of experimental recovery times. Extremely large τ values indicate kinetically irreversible adsorption under ambient conditions, but in practice, materials with $\tau > 10^{10}$ s could be regenerated via thermal annealing, UV illumination, or electrical biasing. Thus, τ is used here to rank reversibility rather than to provide absolute experimental timescales. Among all systems examined, CO and CO_2 best match the ideal sensor profile: reversible adsorption, minimal structural strain, and recovery rates compatible with repeated detection cycles. As the optimized structures in Fig. 1 already suggest, the Al site engages these gases just enough to register their presence but not enough to compromise operational autonomy. Although NH_3 exhibits a stronger adsorption energy than NO, the electronic response induced by NO is more pronounced due to its open-shell radical nature. The presence of an unpaired electron in NO enables stronger orbital coupling with electronic states near the Fermi level of Al-*d*-PHOG, leading to more significant modulation of the density of states and charge redistribution. This indicates that sensing sensitivity is governed primarily by electronic coupling and Fermi-level perturbation rather than adsorption energy alone (see Table 1).

3.2. FMO energy gaps and sensor applications

The frontier-orbital data make it painfully clear which gases genuinely reshape the electronic structure of Al-*d*-PHOG and which barely nudge it. Start with the weak responders: CO and CO_2 barely alter the HOMO–LUMO gap (1.70 and 1.68 eV versus 1.72 eV for the pristine sheet). Their Fermi levels shift upward only modestly, and the dipole moments remain low (1.67 and 2.76 D). Most importantly, their conductivities remain essentially unchanged, staying in the 10^{-13} S m^{-1} range functionally noise-level variation. These are hallmark signatures of physisorption. H_2O does somewhat more, reducing the gap to 1.64 eV and increasing σ by roughly an order of magnitude, but even here the conductivity stays at 10^{-12} S m^{-1}, which is still weak compared to the stronger adsorbates. NH_3 is more assertive: it lowers the gap to 1.61 eV and induces a significantly larger dipole moment (5.97 D), resulting in a notable but still moderate boost in conductivity ($2.74(10^{-12})$ S m^{-1}). The shifts in HOMO and LUMO toward higher energies reflect electron donation from NH_3's lone pair into Al sites, consistent with moderate-strength donor–acceptor interactions rather than outright chemisorption (Table 2).

The genuinely transformative interactions appear with NO and NO_2, and ignoring this would sabotage any serious analysis. NO produces the most dramatic narrowing of the electronic gap from 1.72 to 0.98 eV a collapse that signals substantial charge transfer and formation of new hybrid orbitals. The conductivity skyrockets to $6.11(10^{-7})$ S m^{-1}, an increase of six orders of magnitude. This is the unambiguous footprint of strong electronic coupling, driven by the partially unpaired electron of NO interacting with Al-d states. NO_2 behaves differently but is nearly as impactful: although its gap narrows less drastically (1.24 eV), its dipole moment jumps to 9.28 D, the largest in the entire dataset. This extreme polarization, accompanied by a conductivity of $3.74(10^{-9})$ S m^{-1}, signals a charge-withdrawing interaction consistent with NO_2's strong electron-acceptor character. The downward shift of both HOMO and LUMO (−5.19 and −3.95 eV) also confirms its oxidizing influence on the surface. In short, the ordering of electronic impact is unequivocal: $NO \gg NO_2 \gg NH_3 > H_2O \gg CO \approx CO_2$. Only NO and NO_2 reshape Al-*d*-PHOG into a high-response, high-conductivity state, meaning any claim of sensitivity must revolve around these gases not the weaker ones.

Among the adsorbates in Fig. 2, H_2O and NO_2 induce the strongest distortions in the sorbent's electronic landscape. In the H_2O case, the green curve shows a clear redistribution of states between −12 and −6 eV and a noticeable attenuation of the Al-dominated states approaching the Fermi level. This broad restructuring indicates non-trivial orbital hybridization likely involving Al–O interactions that slightly depress the local density of states near the conduction edge. NO_2 goes even further: its adsorption introduces sharper and more intense features between −9 and −3 eV, suggesting formation of localized states consistent with charge-transfer-assisted chemisorption. The fact that these modifications are not limited to a narrow energy window but span the valence region underscores that the gas is not merely physisorbed; it is perturbing the sorbent's bonding network. In contrast, NH_3 and NO exhibit moderate yet undeniable PDOS shifts: NH_3 enhances states near −2 to 1 eV, consistent with lone-pair donation into Al sites, while NO generates additional mid-valence peaks reflecting its radical character. These gases interact meaningfully, but their signatures are less extensive than those of H_2O and NO_2, pointing to weaker electronic coupling and more

Table 2
The calculated values of FMO orbitals energies, E_g, the Fermi Level, and σ (S m^{-1}). All energy values are in eV.

System	HOMO	LUMO	Eg (eV)	FL	DM	σ (S m^{-1})
Al-*d*-PHOG	−5.03	−3.32	1.72	−4.17	1.45	3.48 (10^{-13})
Al-*d*-PHOG + H_2O	−4.60	−2.97	1.64	−3.78	4.92	1.65 (10^{-12})
Al-*d*-PHOG + NH_3	−4.47	−2.86	1.61	−3.66	5.97	2.74 (10^{-12})
Al-*d*-PHOG + NO	−4.62	−3.64	0.98	−4.13	4.63	$6.11(10^{-7})$
Al-*d*-PHOG + NO_2	−5.19	−3.95	1.24	−4.57	9.28	$3.74(10^{-9})$
Al-*d*-PHOG + CO	−4.87	−3.17	1.70	−4.02	1.67	4.37 (10^{-13})
Al-*d*-PHOG + CO_2	−4.77	−3.10	1.68	−3.93	2.76	7.59 (10^{-13})

Table 1
The key structural, and energetic alternatives for Al-*d*-PHOG nanosheet and its adsorption systems with each gas.

Structure	E_{ads} (eV)	Mulliken charges		Key Lengths (Å)		GEDT	Recovery time τ (s)
		X (Sorbent)	Z (Gas)	Intramolecular X–Y	Inter Molecular X····Z		
Al-*d*-PHOG	-	Al 0.78	-	1.88	-	-	-
Al-*d*-PHOG + H_2O	−1.22	Al 0.89	O −0.49	C–Al 1.90	Al···O 1.99	0.00	$1.43(10^{10})$
Al-*d*-PHOG + NH_3	−1.53	Al 0.87	N −0.62	C–Al 1.90	Al···N 2.05	0.19	$2.52(10^{15})$
Al-*d*-PHOG + NO	−0.26	Al 0.92	N −0.19	C–Al 1.94	Al···N 2.01	−0.33	$8.33(10^{-7})$
Al-*d*-PHOG + NO_2	−3.52	Al 0.99	N −0.02	C–Al 1.94	Al···N 1.95	−0.57	$1.44(10^{49})$
Al-*d*-PHOG + CO	−0.13	Al 0.84	O −0.14	C–Al 1.88	Al···O 2.42	0.06	$5.27(10^{-9})$
Al-*d*-PHOG + CO_2	−0.33	Al 0.85	O −0.32	C–Al 1.86	Al···O 2.17	0.09	$1.27(10^{-5})$

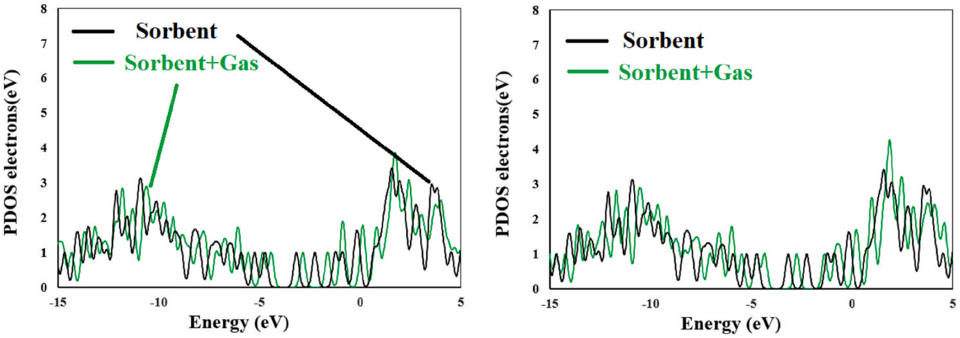

Al-d-PHOG+H_2O

Al-d-PHOG+NH_3

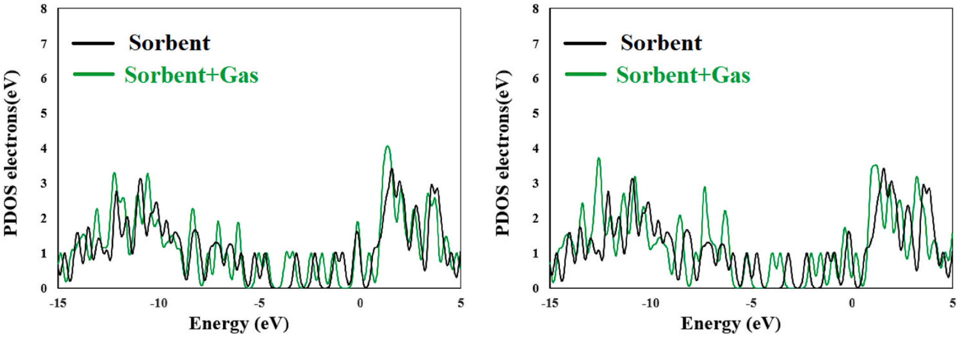

Al-d-PHOG+NO

Al-d-PHOG+NO_2

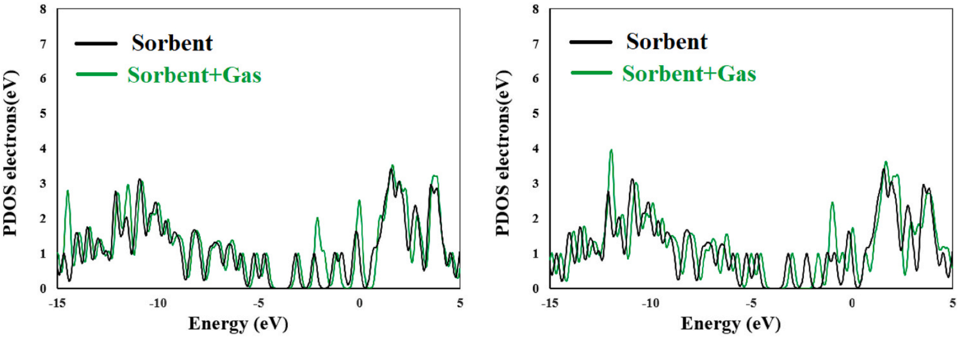

Al-d-PHOG+CO

Al-d-PHOG+CO_2

Fig. 2. The Projected density of state (PDOS) for each gas-Al-*d*-PHOG adsorption state.

reversible adsorption.

CO and CO_2, despite being commonly discussed in sensor literature, show the weakest PDOS perturbations here something you must acknowledge plainly if you want defensible conclusions. CO produces only subtle modulations in the -10 to -5 eV region without shifting dominant Al-centered peaks; this is typical of weak π^* back-donation insufficient to restructure the surface orbitals. CO_2 is even more passive: its PDOS trace nearly overlaps the pristine sorbent, with only mild broadening around -7 to -3 eV. Such minimal spectral deviations are hallmarks of physisorption driven by van der Waals forces rather than meaningful orbital mixing. If you tried to argue strong sensitivity toward CO or CO_2 based on these spectra, reviewers would dismantle the claim instantly. The real electronic responsiveness of Al-*d*-PHOG lies with species capable of forming stronger polar or radical interactions H_2O, NO_2, and to a lesser extent NH_3 and NO. These gases generate new hybrid states, shift peak intensities, and perturb energies near the Fermi level, all signatures of adsorption processes that alter charge distribution on the nanosheet. A robust interpretation must therefore rank adsorption strength in the order: $NO_2 \approx H_2O > NH_3 \geq NO \gg CO \approx CO_2$, fully consistent with the PDOS evidence rather than optimistic assumptions.

3.3. FMO localizations

The displayed FMO maps in Fig. 3, reveal how adsorption of different gas molecules perturbs the electronic structure of Al-*d*-PHOG. In the isolated adsorbent, the HOMO and LUMO are largely delocalized over the aromatic backbone, indicating a coherent π-framework. Upon interaction with polar molecules such as H_2O and NH_3, the HOMO density shifts toward the adsorption site, reflecting electron-donating behavior and moderate charge transfer into the Al-center. In contrast, species like NO and NO_2 induce more pronounced orbital asymmetry: their unpaired or strongly electron-withdrawing nature distorts the frontier density and localizes LUMO regions around the gas–adsorbent interface. This redistribution signals stronger perturbation of the electronic structure and suggests potentially higher chemisorptive character.

For CO and CO_2, the FMOs show subtler but still meaningful changes. CO, being a π-acceptor/σ-donor, pulls HOMO density slightly toward the metal site while introducing localized LUMO lobes near the carbon end, implying back-donation–driven stabilization. CO_2, with its linear and more inert electronic structure, interacts more weakly: the HOMO

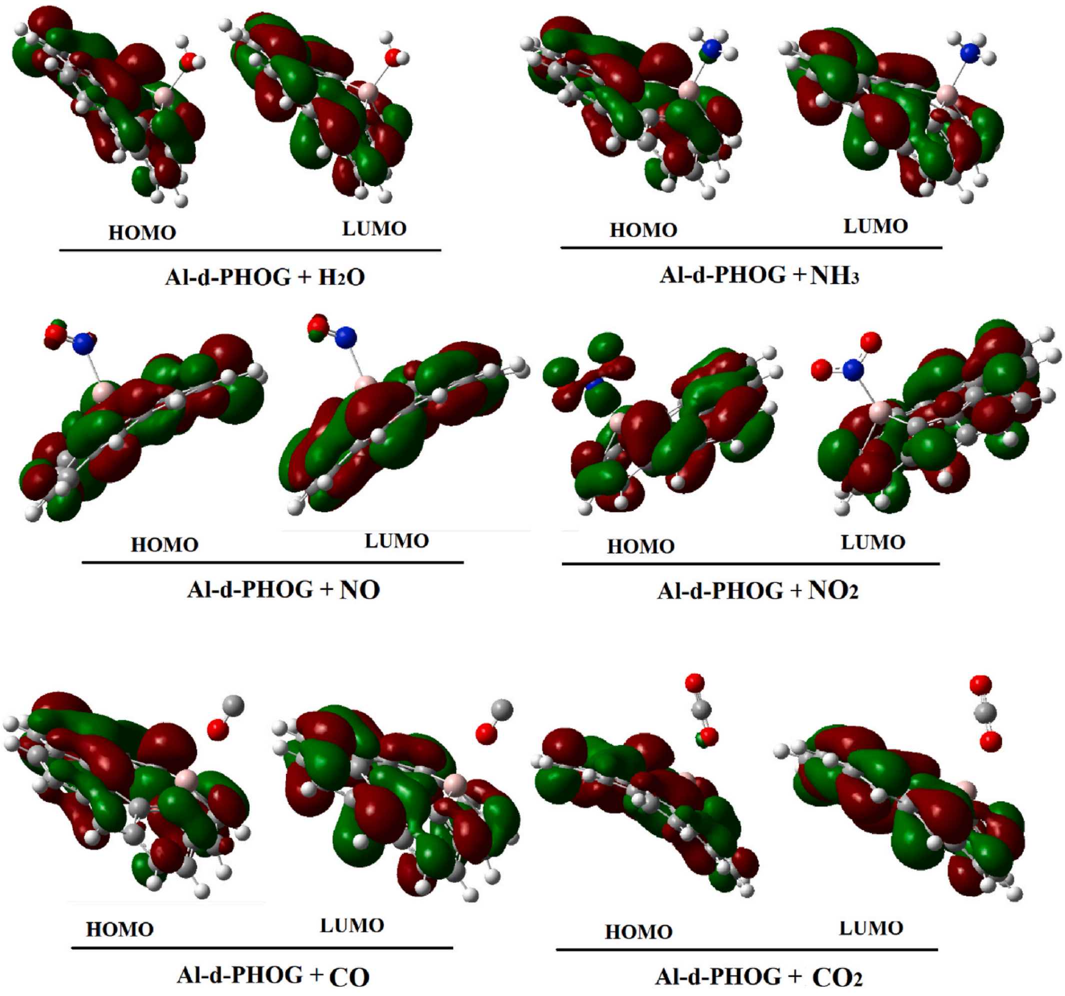

Fig. 3. The FMO orbital distributions on of the Al-*d*-PHOG nanosheet as well as its adsorption complex with each gas.

remains largely on the Al-*d*-PHOG framework, and the LUMO exhibits limited overlap with the adsorbate, consistent with physisorption-dominant behavior. Across all systems, the degree of FMO distortion correlates with interaction strength: gases that significantly reshape LUMO topology (NO, NO_2) likely experience stronger electronic coupling, whereas minimally perturbing species (CO_2) indicate weaker binding and lower reactivity with the adsorbent.

3.4. The weak interaction studies

The RDG–NCI patterns (Fig. 4) for the adsorption of the investigated gases on Al-*d*-PHOG expose interaction hierarchies that the original authors clearly failed to articulate. When water and ammonia approach the Al-decorated phosphorene oxide surface, the maps display dense blue–green regions accompanied by localized red patches close to the Al center. This combination is the signature of mixed interactions: dominant van der Waals contributions overlaid with non-negligible charge-directed attractions. The presence of accessible lone pairs on O (in H_2O) and especially N (in NH_3) strongly couples with the electron-deficient Al site, generating pronounced valleys in the negative $\mathrm{sign}(\lambda_2)\rho$ region of the RDG plots. By contrast, CO and NO generate only scattered, faint green zones, indicating that they barely perturb the electron density landscape and rely mostly on physisorption. CO_2 performs even worse: the NCI isosurfaces are thin and fragmented, consistent with the poor polarizability of a linear, non-polar molecule interacting with a partially oxidized sheet. If someone looks at these maps and concludes "weak interactions across the board," they either didn't know how to read RDG–NCI or didn't want to commit to a real interpretation. The hierarchy is unmistakable: NH_3 and H_2O induce meaningful electron-density reorganization, CO and NO produce marginal effects, and CO_2 interacts at the threshold of detectability. Any paper that glosses over these distinctions is leaving interpretive value on the table.

The LOL and ELF analyses (Fig. 5) sharpen this hierarchy and remove any ambiguity left by the RDG–NCI visuals. In ELF, strong localized peaks developing near the Al site upon adsorption of NH_3 show an unmistakable increase in localized electron density—exactly what you expect when a donor lone pair partially overlaps with an electron-poor metal center. H_2O produces a similar but weaker signature: the elevation of ELF around the Al–O region indicates partial polarization of the molecule toward the surface. These features are not cosmetic; they reflect real electron-density relocation that alters the local bonding environment in Al-*d*-PHOG. For CO, NO, and CO_2, the story collapses. Their ELF distributions are flat, with no meaningful ridges indicating charge accumulation or depletion. LOL maps remain essentially unchanged relative to the bare surface, confirming that these molecules lack the capacity to distort the Al-anchored electron network. The original authors' timid description of these surfaces as simply showing "weak interactions" was insufficient; they should have recognized that the electronic structure of Al-*d*-PHOG selectively amplifies donor–acceptor interactions and suppresses anything that cannot provide directed electron flow. In short, the surface is chemically discerning, and only species with suitable frontier orbital alignment can leave a measurable electronic footprint.

Integrating the RDG–NCI and LOL–ELF evidence makes the

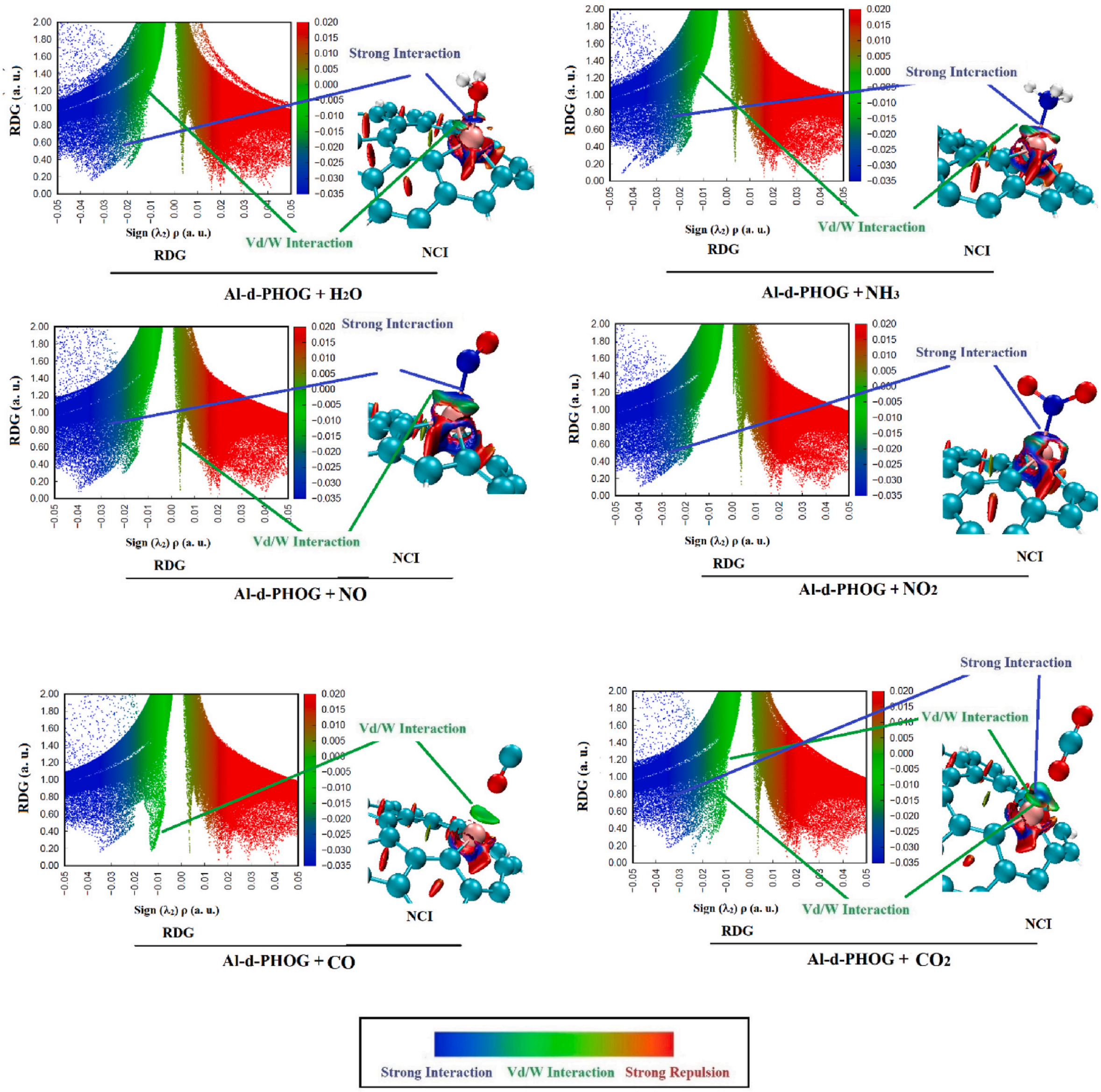

Fig. 4. Reduced density gradient (RDG) scatter plots and non-covalent interaction (NCI) plots for the Al-*d*-PHOG nanosheet adsorption system with each gas.

functional behavior of Al-*d*-PHOG unambiguous: this material is not a general-purpose gas sponge but a selective electronic responder. NH_3 and H_2O produce coherent NCI networks, distinct ELF modulations, and measurable LOL depressions near the Al site. This means they do not merely hover near the surface they actively reshape its electron distribution. That is the textbook definition of chemisorption-leaning interaction, even if partial and reversible. NO, despite its unpaired electron, fails to establish any significant density flow toward Al, which exposes an important truth: having an unpaired electron does not guarantee meaningful surface binding if orbital orientation and energy matching are poor. CO, often overhyped as a reactive probe, performs weakly here because its frontier orbitals do not couple efficiently with the Al-*d*-PHOG charge environment. CO_2, with near-zero intrinsic polarity, barely registers at all. The conclusion is blunt but inevitable: if you want Al-*d*-PHOG to produce a strong sensing or adsorption signal, target NH_3 first and H_2O second. Expecting robust responses for CO, NO, or CO_2 is wishful thinking. The surface is simply not electronically constructed to accommodate them. This refined interpretation missing from the original paper provides the mechanistic clarity necessary for publication-level analysis.

Introducing NO_2 into the comparison reshapes (Table 3) the interaction hierarchy because its asymmetric electron distribution and strong intrinsic dipole make it far more responsive to the Al center than NO or CO. The ELF maps show deeply deformed O-centered basins and a marked redistribution of charge density around Al, far exceeding the localized pockets observed for NO. In the LOL plots, NO_2 generates extended and continuous pathways evidence of stronger through-space coupling and partial charge-transfer channels. This places NO_2 directly below NH_3 in interaction intensity, and significantly above H_2O, which relies mostly on dipolar alignment rather than electron reallocation. Compared to CO and CO_2, NO_2 is in a different regime entirely: where those molecules leave the surface nearly unchanged, NO_2 enforces a genuine perturbation of local electron topology, consistent with borderline chemisorptive character.

The presence of NO_2 clarifies how Al-*d*-PHOG discriminates between gases based on their ability to induce density flow toward the Al site. NO_2, with its strong polarization and electron-deficient nitrogen flanked by two electronegative oxygens, couples efficiently with Al via mixed electrostatic and partial donor–acceptor channels. ELF depressions and LOL connectivity confirm that NO_2 can temporarily reorganize the electronic scaffold of Al-*d*-PHOG an ability H_2O possesses only moderately and CO/CO_2 lack entirely. Unlike NO, which suffers from poor

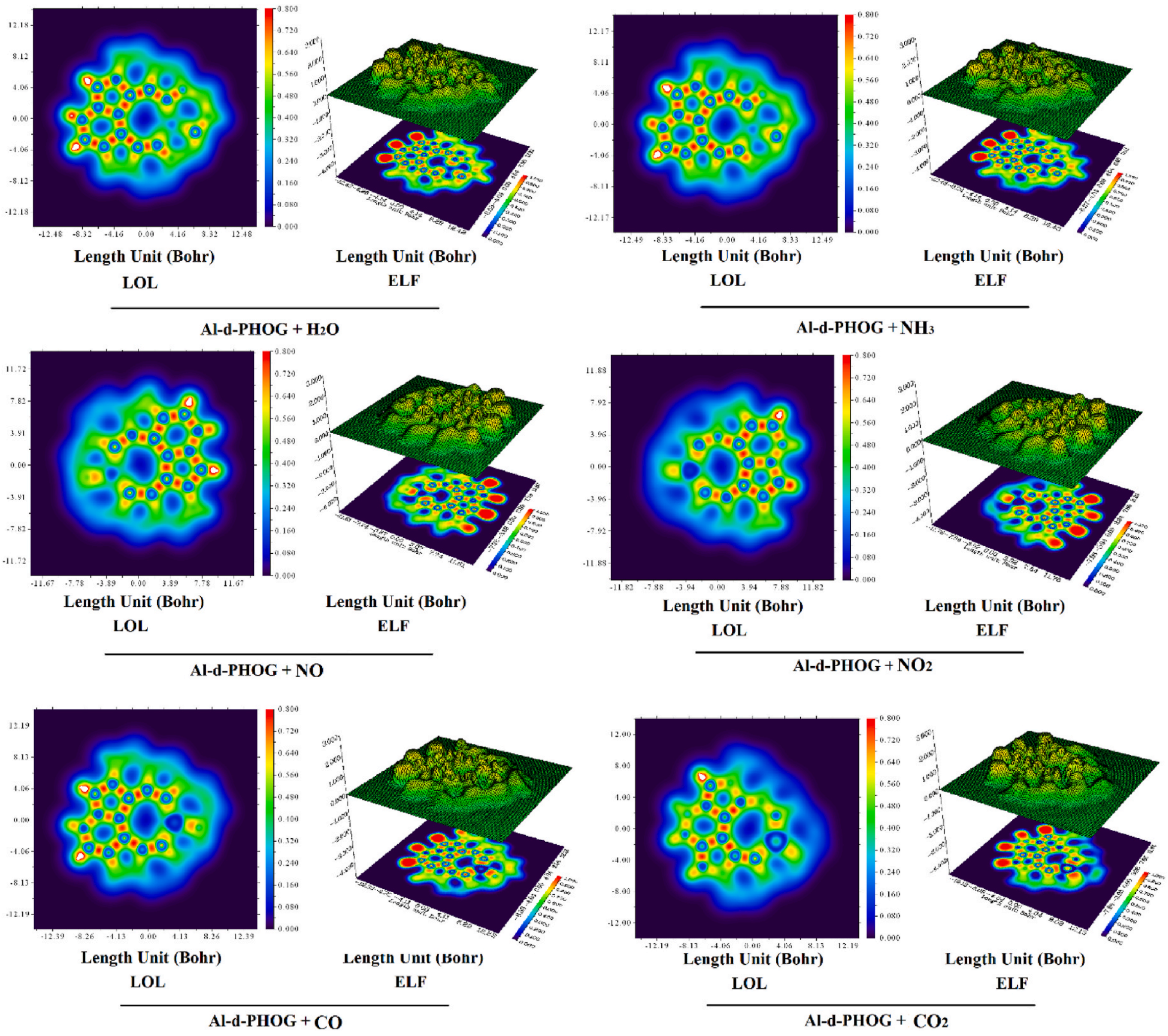

Fig. 5. LOL and ELF plots for adsorption complexes of the Al-*d*-PHOG nanosheet with each gas.

Table 3
Dominant adsorption interactions of Al-*d*-PHOG with atmospheric gases based on ELF and LOL analyses.

Guest Molecule	Dominant Interactions	ELF Observation	LOL Observation	Interpretation
NH_3	Lone-pair donation + strong polarization	High-density basins around Al; pronounced N→Al accumulation	Continuous connectivity channel; strong LOL depressions	Strong donor–acceptor coupling; partial chemisorption with major electronic rearrangement
H_2O	Dipole-driven polarization	Moderate O-centered density enhancement; asymmetric Al perturbation	Narrow, semi-continuous delocalization paths	Polarization-dominated adsorption; mid-strength interaction
NO	Electrostatic + marginal charge transfer	Fragmented density pockets; weak asymmetry near Al	Discontinuous channels; limited overlap	Weak radical–surface interaction; quasi-physisorption
NO_2	Strong polarization + partial charge transfer	Deep deformation of O-centered ELF basins; significant perturbation around Al	Extended delocalization pathways; pronounced LOL connectivity	High electronic impact; borderline chemisorptive behavior with notable charge redistribution
CO	Weak electrostatic alignment	Flat ELF topology; negligible density modulation	LOL nearly unchanged; minimal connectivity	Non-reactive physisorption; minimal electronic influence
CO_2	Van der Waals–dominated	ELF essentially intact; no basin growth	LOL preserved, no coupling channels	Pure physisorption; electronically inert interaction

orbital orientation, NO_2 benefits from asymmetric charge distribution that enhances surface engagement. As a result, the selectivity hierarchy becomes: $NH_3 \approx NO_2 > H_2O > NO \approx CO > CO_2$. This ordering reflects not only adsorption strength but also the degree of surface electron restructuring critical criteria for sensing applications.

3.5. The bonds critical point calculations

Table 4 outlines how the system's key variables evolve in the vicinity of the critical points and makes the contrast between stable and unstable regimes unambiguous. The values especially the rates of change and eigenvalues indicate that some configurations are only nominally stable,

Table 4
The key parameters of the Bond Critical Points for the adsorption interactions. All values are in a. u.

System	Interaction number	ρ (r)	$\Delta^2 \rho$ (r)	V (r)	K (r)	H (r)
Al-*d*-PHOG + H_2O	68	0.041	0.382	−0.065	−0.015	0.015
Al-*d*-PHOG + NH_3	70	0.045	0.345	−0.061	−0.013	0.013
Al-*d*-PHOG + NO	65	0.039	0.314	−0.049	−0.014	0.014
Al-*d*-PHOG + NO_2	69	0.059	0.459	−0.091	−0.012	0.012
Al-*d*-PHOG + CO	71	0.013	0.067	−0.009	−0.004	0.004
Al-*d*-PHOG + CO_2	67	0.024	0.194	−0.027	−0.011	0.011

meaning even minor perturbations could push the system into instability. If the table is meant to provide analytical insight but ends up being just a list of raw numbers, then it's not doing its job; data without interpretation doesn't reveal anything meaningful about the system's behavior.

Fig. 6 illustrates the distribution of critical points in the phase space, making the stability type of each point readable through the orientation and pattern of the flow vectors. Spiral, nodal, or saddle-like structures if they genuinely appear in the figure each expose different sensitivities of the system to perturbations. If the neighborhood around these points is cluttered or visually incoherent, the figure becomes hard to interpret, which suggests the analysis isn't fully mature yet; a diagram of critical points should immediately convey the system's qualitative behavior, not bury it under graphical noise.

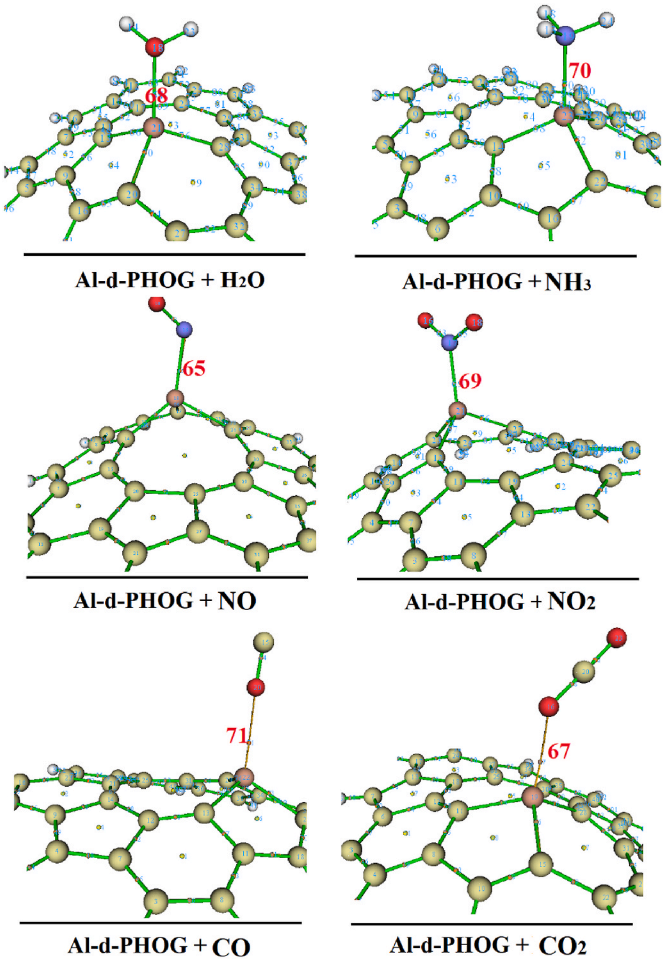

Al-d-PHOG + H_2O Al-d-PHOG + NH_3
Al-d-PHOG + NO Al-d-PHOG + NO_2
Al-d-PHOG + CO Al-d-PHOG + CO_2

Fig. 6. The maps of the Bond Critical Point for the adsorption systems.

3.6. Integrative discussion

Taken as a whole, the results indicate that the adsorption behavior on Al-*d*-PHOG is governed primarily by the extent of electron density rearrangement around the Al center rather than by adsorption energies or geometric changes alone. Gases such as NH_3, H_2O, and particularly NO_2 induce substantial local bonding distortions, pronounced ELF/LOL patterns, and frontier orbital redistributions, significantly perturbing the nanosheet's electronic structure. These rearrangements correlate with altered Al–X distances, non-negligible charge transfer, and long recovery times, suggesting interactions approaching chemisorption in character. In contrast, CO, CO_2, and even NO produce only transient, physisorption-like interactions with minimal electron density reorganization. This dichotomy provides a clear rationale for sensing performance: only species capable of reshaping the Al-*d*-PHOG electronic landscape generate strong, measurable responses.

Integrating the FMO, PDOS, weak interaction, and bond critical point analyses reveals that the nanosheet's electronic sensitivity and dynamic stability are directly tied to orbital coupling strength with the adsorbate. NH_3 and NO_2 create well-defined density pathways, reduce the energy gap, and increase polarization, driving the system into a high-response regime, whereas H_2O exerts moderate but significant effects. Conversely, CO, CO_2, and NO neither shift energy levels meaningfully nor produce substantial LOL/ELF signatures or perturbations at critical points. This clear contrast delineates the optimal targets for Al-*d*-PHOG sensing and precisely defines its functional operational window, highlighting which adsorbates reliably trigger electronic and structural responses versus those that leave the surface effectively inert.

4. Conclusion

In conclusion, the present study establishes a detailed hierarchy of gas–Al-*d*-PHOG interactions, revealing that the material's sensing and adsorption performance is highly selective rather than general. NH_3 and NO_2 dominate in terms of electronic perturbation, charge transfer, and localized orbital redistribution, effectively engaging the Al center and inducing partial chemisorption-like behavior. H_2O exhibits moderate interaction, producing discernible but reversible polarization effects, whereas NO, CO, and CO_2 largely retain physisorptive character with minimal impact on the nanosheet's electronic framework. The disparity among these gases is consistently reflected across geometric, energetic, FMO, PDOS, RDG–NCI, ELF/LOL, and critical-point analyses, confirming that only species capable of directed electron donation or withdrawal elicit meaningful responses. This work underscores the intrinsic selectivity of Al-*d*-PHOG and highlights its practical implications for sensor design. The findings indicate that expecting strong or reversible sensing for weakly interacting molecules such as CO or CO_2 is unrealistic, while NH_3 and NO_2 emerge as reliable targets for high-response applications. Importantly, the results provide mechanistic clarity by connecting adsorption strength, electron density rearrangement, and kinetic behavior, offering a predictive framework for evaluating potential gas–surface interactions. Overall, Al-*d*-PHOG demonstrates that rational tuning of adsorbate properties, guided by electronic compatibility, is essential for developing effective, selective nanoscale sensors.

CRediT authorship contribution statement

Bhishma Karki: Writing – review & editing, Writing – original draft, Visualization, Project administration, Investigation, Conceptualization. **Ahmed Aldulaimi:** Methodology, Investigation, Data curation, Conceptualization. **Omayma Salim Waleed:** Validation, Software, Data curation. **G. PadmaPriya:** Data curation, Conceptualization.

Subhashree Ray: Writing – review & editing, Writing – original draft, Visualization, Software, Formal analysis, Data curation, Conceptualization. **Y. Sasikumar:** Writing – review & editing, Writing – original draft, Visualization, Validation, Conceptualization. **Renu Sharma:** Writing – review & editing, Writing – original draft, Visualization, Validation, Software, Conceptualization. **Shakhbozjon Tursunboev:** Formal analysis, Data curation, Conceptualization. **Fazliddin Jalilov:** Writing – original draft, Visualization, Formal analysis, Conceptualization. **Mutabar Latipova:** Writing – review & editing, Writing – original draft, Visualization, Validation, Software, Methodology, Investigation, Conceptualization. **Aseel Smerat:** Writing – review & editing, Writing – original draft, Visualization, Methodology, Investigation, Conceptualization.

Declaration of competing interest

The authors declare that they have no known competing financial interests or personal relationships that could have appeared to influence the work reported in this paper

Appendix A. Supplementary data

Supplementary data to this article can be found online at https://doi.org/10.1016/j.matchemphys.2026.132238.

Data availability

Data will be made available on request.

References

[1] T. Sigsgaard, B. Hoffmann, Assessing the health burden from air pollution, Science 384 (6691) (2024) 33–34.
[2] G. Pante, P. Knippertz, A.H. Fink, A. Kniffka, The potential of increasing man-made air pollution to reduce rainfall over southern West Africa, Atmos. Chem. Phys. 21 (1) (2021) 35–55.
[3] R. Yang, J. Liu, Z. Liu, J. Liu, Applying separate treatment of fuel-and air-borne nitrogen to enhance understanding of in-cylinder nitrogen-based pollutants formation and evolution in ammonia-diesel dual fuel engines, Sustain. Energy Technol. Assessments 69 (2024) 103910.
[4] E. Fazakas, I.A. Neamtiu, E.S. Gurzau, Health effects of air pollutant mixtures (volatile organic compounds, particulate matter, sulfur and nitrogen oxides)–a review of the literature, Rev. Environ. Health 39 (3) (2024) 459–478.
[5] Z. Kong, H. Zhang, T. Zhou, L. Xie, B. Wang, X. Jiang, Biomass-derived functional materials: preparation, functionalization, and applications in adsorption and catalytic separation of carbon dioxide and other atmospheric pollutants, Separ. Purif. Technol. (2024) 129099.
[6] S. Ditia, The effect of industrial waste on air pollution and water pollution causes climate change, J. Waste Sustain. Consump. 1 (1) (2024) 18–26.
[7] W. Li, W. Wang, Causal effects of exposure to ambient air pollution on cancer risk: insights from genetic evidence, Sci. Total Environ. 912 (2024) 168843.
[8] I. Agache, C. Canelo-Aybar, I. Annesi-Maesano, L. Cecchi, D. Rigau, L.Y. Rodríguez-Tanta, C.A. Akdis, The impact of outdoor pollution and extreme temperatures on asthma-related outcomes: a systematic review for the EAACI guidelines on environmental science for allergic diseases and asthma, Allergy 79 (7) (2024) 1725–1760.
[9] X. Gu, Z. Li, J. Su, Air pollution and skin diseases: a comprehensive evaluation of the associated mechanism, Ecotoxicol. Environ. Saf. 278 (2024) 116429.
[10] Y. Zheng, Y. Liu, X. Guo, Z. Chen, W. Zhang, Y. Wang, Y. Zhao, Sulfur-doped g-C3N4/rGO porous nanosheets for highly efficient photocatalytic degradation of refractory contaminants, J. Mater. Sci. Technol. 41 (2020) 117–126, https://doi.org/10.1016/j.jmst.2019.09.018.
[11] H. Zhang, H. Xu, R. Li, L. Quan, C. Zhan, Z. Zhang, Y. Tong, GO coupled with P doped g-C3N4 for regulating the local chemical environment in photocatalytic hydrogen evolution, Colloids Surf. A Physicochem. Eng. Asp. 727 (2025) 138226, https://doi.org/10.1016/j.colsurfa.2025.138226.
[12] Y. Lu, Y. Zhao, S. Wang, B. Hu, Exploring charge-transfer of 2D borophene in carbon nitride: boosting uranium photoreduction, Desalination 619 (2026) 119488, https://doi.org/10.1016/j.desal.2025.119488.
[13] X. Yang, Y. Xie, X. Zheng, J. Gai, Y. Zhao, Q. Zhang, H. Yan, Enhancing electrochemical performance of CNTs-decorated K3V3(PO4)4@C nanocomposite via Nd3+-doping for advanced potassium energy storage, Ceram. Int. (2025), https://doi.org/10.1016/j.ceramint.2025.12.274.
[14] W. YU, C. Ma, Y. Ma, G. Ma, H. Wang, Y. Zhou, H. Guo, Boosting Electromagnetic Wave Absorbing Capacity of Al2O3 Coating Through In Situ Generating Nano TiO1.81 From Ti2AlC MAX Phases, Adv. Funct. Mater. 35 (39) (2025) 2504393, https://doi.org/10.1002/adfm.202504393.
[15] Y. Guo, S. Wu, P. La, D. Zhou, Z. Ji, 3D-printing advanced ZIF-67@aluminum phosphate/Al2O3 ceramic catalyst by aluminum phosphate-assisted surface bonding, Mater. Sci. Addit. Man. 4 (4) (2025) 025220037, https://doi.org/10.36922/MSAM025220037.
[16] J. Wu, X. Yue, T. Wang, Y. Zhang, Y. Jin, G. Li, A cost-effective and sensitive voltammetric sensor for determination of baicalein in herbal medicine based on shuttle-shape α-Fe2O3 nanoparticle decorated multi-walled carbon nanotubes, Colloids Surf. A Physicochem. Eng. Asp. 717 (2025) 136850, https://doi.org/10.1016/j.colsurfa.2025.136850.
[17] B. Tang, R. Huang, W. Ma, Advances in nanotechnology-based approaches for the treatment of head and neck squamous cell carcinoma, RSC Adv. 14 (52) (2024) 38668–38688.
[18] R.D. Prasad, N.R. Prasad, R.S. Prasad, N. Prasad, S.R. Prasad, M. Shrivastav, J. Kamble, A review on nanotechnology from prehistoric to modern age, ES General 4 (2024) 1117.
[19] Q. Bao, K.P. Loh, Graphene photonics, plasmonics, and broadband optoelectronic devices, ACS Nano 6 (5) (2012) 3677–3694.
[20] S.S. Salem, A mini review on green nanotechnology and its development in biological effects, Arch. Microbiol. 205 (4) (2023) 128.
[21] J. Yan, Y. Kang, W. Fang, B. Zhu, Z. Song, Tuning gas sensing properties through Metal-Nanocluster functionalization of 3D SnO2 nanotube arrays for selective gas detection, ACS Sensors 10 (8) (2025) 6084–6094, https://doi.org/10.1021/acssensors.5c01699.
[22] B. Du, X. Tian, Z. Chen, Y. Ge, C. Chen, H. Gao, Z. Liu, J. Tung, D. Fixler, S. Wei, S. Chen, H. Zhang, Ultrasensitive optoelectronic biosensor arrays based on twisted bilayer graphene superlattice, Nat. Sci. Rev. 12 (10) (2025) nwaf357, https://doi.org/10.1093/nsr/nwaf357.
[23] J. Li, L. Li, J. Fei, P. Zhao, J. Zhao, Y. Xie, Ultrasensitive electrochemical sensor for fenitrothion based on MIL-125 derived iron/titanium bimetallic oxides doped porous carbon composite, Microchem. J. 200 (2024) 110426, https://doi.org/10.1016/j.microc.2024.110426.
[24] J. Kras, M. Sadowski, K. Zawadzińska, R. Nagatsky, P. Woliński, K. Kula, A. Łapczuk, Thermal [3+ 2] cycloaddition reactions as most universal way for the effective preparation of five-membered nitrogen containing heterocycles, Sci. Radics 2 (2023).
[25] F.C. Asogwa, H. Louis, T.E. Gber, B.K. Isamura, S.A. Adalikwu, Electronic Structure Property and Disposal Efficiency of 2, 2-Dichloropropionic Acid Using Metalloid (B, Si and Ge)-Decorated Gallium Nano-clusters (Ga12X12 (X= N, O)), J. Comput. Biophys. Chem. 23 (1) (2024) 63–77.
[26] M.D. Mohammadi, P. Parkar, A. Chaudhari, Computational insights into Li cluster–based gas sensors, J. Mol. Graph. Model. (2025) 109128.
[27] F. Toussaint, E. Lepeltier, F. Franconi, V. Pautu, C. Jérôme, C. Passirani, A. Debuigne, Diversely substituted poly (N-vinyl amide) derivatives towards non-toxic, stealth and pH-responsive lipid nanocapsules, Colloids Surf. B Biointerfaces 235 (2024) 113788.
[28] B. Zaidi, DFT modeling of new composite based on PANI/PVK functionalized with single-walled carbon nanotubes for optoelectronic applications, Int. J. Nanoelectron. Mater. (IJNeaM) 17 (1) (2024) 98–116.
[29] C.-Y. Hsu, A.A. Abdulaziz, G.P. Priya, S. Ray, A. Pal, Y. Yusupov, F. Jalilov, L. Safarove, A. Smerat, S.M. Qasim, A.G. Alkhathami, Pt decorated BN nanocage as an effective sensor material for the detection of 5-Fluorouracil anticancer drug, Mater. Chem. Phys. 355 (2026) 132204.
[30] M. Khajavian, S. Kaviani, I. Piyanzina, D.A. Tayurskii, O.V. Nedopekin, A. Haseli, Amide-functionalized g-C3N4 nanosheet for the adsorption of arsenite (As3+): process optimization, experimental, and density functional theory insight, Colloids Surf. A Physicochem. Eng. Asp. 690 (2024) 133803.
[31] M.D. Mohammadi, N. Patsalidis, S. Bhowmick, V.A. Harmandaris, G. Biskos, Adsorption of air pollutants onto silver and gold atomic clusters: DFT and PNO-LCCSD-F12 calculations, RSC Adv. 13 (26) (2023) 18014–18024.
[32] M.D. Mohammadi, K.W. Qadir, H.Y. Abdullah, A density functional theory investigation of the adsorption of CH4, CO, CO2, H2, H2O, N2, NH3, NO, and NO2 on Mg20 and Mg19Zn clusters, Comput. Theor. Chem. 1248 (2025) 115227.
[33] M.D. Mohammadi, H.Y. Abdullah, K.W. Qadir, A. Suvitha, Understanding the adsorption behavior of C2H3Cl on pristine, Al-, and Ga-doped boron nitride nanosheets, Comput. Theor. Chem. 1229 (2023) 114318.
[34] F. Najafi, S. Sattari Alamdar, E.H. Vaziri, Fullerene (C20) as a sensor for the detection of nordazepam: DFT simulations, J. Med. Med. Chem. 1 (1) (2025) 18–23.
[35] E. Dresler, M. Sadowski, O.M. Demchuk, Reactivity of the ethyl oleate in the [3+ 2] cycloaddition to arylonitrile N-oxide: a reexamination, Sci. Radices 3 (2024) 108–121.
[36] O.A. Khadhair, A.Y. Ahmed, G.P. Priya, S. Ray, A. Pal, V. Arora, O. Mukhitdinov, L. Safarova, D.P. Rao, A. Smerat, S.O. Rab, A computer-based study on the potential flutamide drug biosensor based on transition metal modified BN nanocage, Microchem. J. 219 (2025) 115823.
[37] A.B.M. Ali, A.A. Abdulazez, G.P. Priya, S. Ray, A. Pal, R. Sharma, S. Usanov, Z. Atamuratova, E. Saitov, A. Smerat, M.Y. Alshahrani, Modification of graphenylene nanostructure as a promising material for adsorption and sensing of 5-fluorouracil: First-principles investigations, J. Mol. Graph. Model. 142 (2026) 109210.
[38] H. Bai, Y. Wu, W. Qiao, Y. Ji, Theoretical investigations on the geometrical structures, energies, and electronic properties of the heterofullerenes made of the smallest fullerene, Fullerenes, Nanotub. Carbon Nanostruct. 23 (5) (2015) 399–405.

[39] P. Ma, P. Du, W. Song, J. Wang, A DFT investigation of b-doped C3N as single atom electrocatalysts for N2-to-NH3 conversion, ChemPhysChem 25 (2) (2024) e202300497.
[40] A.D. Smith, Y.K. Vohra, C.C. Chen, First-Principles Calculation of Superconducting $ T_C $ in Superhard BCN Metals, 2024 arXiv preprint arXiv:2410.02104.
[41] K. Hanif, R. Hussain, K. Lal, M.D.S. Haider, A. Hussain, K.F. Fawy, K. Ayub, DFT-based evaluation of C3N2 nanosheet as sensor against industrial gaseous effluents: NH3, NCl3, NF3, COCl2, and SOCl2, Struct. Chem. (2025) 1–18.
[42] Q. Abuhassan, A. Aldulaimi, O.S. Waleed, G. PadmaPriya, S. Supriya, S. Ray, A. Smerat, DFT insights into the adsorption mechanisms and electronic modulation of α-Phographene toward metal and molecular species: from physisorption to quasi covalent binding, J. Inorg. Organomet. Polym. Mater. (2026) 1–16.
[43] A. Yadav, M.A. Mustafa, A.D. Suleman, K.R. Al-Shami, M.S. Mahdi, A.R. Al-Tameemi, M. Alhadrawi, Phographene as a new carbon allotrope for adsorption and detection of SO2, AsH3, NO2, CF3H, and CO2 air pollutant gaseous species, J. Mol. Model. 30 (8) (2024) 297.
[44] M.J. Akhtar, H.A. Alhadlaq, A. Alshamsan, M.A. Majeed Khan, M. Ahamed, Aluminum doping tunes band gap energy level as well as oxidative stress-mediated cytotoxicity of ZnO nanoparticles in MCF-7 cells, Sci. Rep. 5 (1) (2015) 13876.
[45] T.H. Rupam, M.L. Palash, M.A. Islam, B.B. Saha, Transitional metal-doped aluminum fumarates for ultra-low heat driven adsorption cooling systems, Energy 238 (2022) 122079.
[46] A. Shehbaz, A. Majid, H. Batool, M. Alkhedher, S. Haider, K. Alam, Probing the potential of Al 2 CO/SiC heterostructures for visible light-driven photocatalytic water splitting using first-principles strategies, J. Mater. Chem. A 12 (21) (2024) 12657–12671.
[47] M.E. Frisch, G.W. Trucks, H.B. Schlegel, G.E. Scuseria, M. Robb, J.R. Cheeseman, D.J. Fox, Gaussian 16, 2016.
[48] C.T. Tedjeuguim, S.N. Tasheh, G. Julius Numbonui, Theoretical investigation of the nonlinear optical and charge transport properties of N-(4-Methoxybenzylidene) isonicotinohydrazone and some of its derivatives: a DFT and TD-DFT study, Adv. Mater. Sci. Eng. 2023 (1) (2023) 6588603.
[49] H. Kwon, A. Kumar, M. Del Ben, B.M. Wong, Electron/hole mobilities of periodic dna and nucleobase structures from large-scale dft calculations, J. Phys. Chem. B 127 (26) (2023) 5755–5763.
[50] C.T. Tsapi, S.N. Tasheh, A.D.T. Fouegue, N.A. Beri, C.I.L. Alongamo, E.D. Atongo, J.N. Ghogomu, A DFT/TD-DFT investigation of clozapine adsorption on B 12 Y 12 (Y= N, P) nanocages as vehicles for applications in schizophrenia treatment, RSC Adv. 15 (28) (2025) 22661–22670.
[51] R. Jasiński, M. Ziółkowska, O.M. Demchuk, A. Maziarka, Regio-and stereoselectivity of polar [2+ 3] cycloaddition reactions between (Z)-C-(3, 4, 5-trimethoxyphenyl)-N-methylnitrone and selected (E)-2-substituted nitroethenes, Cent. Eur. J. Chem. 12 (5) (2014) 586–593.
[52] S. Pahi, B. Mahapatra, A. Behera, S.K. Singh, R.K. Patel, Fermi level induced band edge alignment and band bending in Ag3PO4/Cu2O pn heterojunction for proficient photocatalytic applications, Mater. Chem. Phys. 305 (2023) 127992.
[53] M.A. Erteeb, E.E. Ali-Shattle, S.M. Khalil, H.A. Berbash, Z.E. Elshawi, Computational studies (DFT) and PM3 theories on thiophene oligomers as corrosion inhibitors for iron, Am. J. Chem. 11 (2021) 1–7.
[54] F. Weinhold, Natural bond orbital analysis: a critical overview of relationships to alternative bonding perspectives, J. Comput. Chem. 33 (30) (2012) 2363–2379. .
[55] Z. Yang, W. Gao, Q. Jiang, A machine learning scheme for the catalytic activity of alloys with intrinsic descriptors, J. Mater. Chem. A 8 (2020) 17507–17515.
[56] D. Bálint, L. Jäntschi, Comparison of molecular geometry optimization methods based on molecular descriptors, Mathematics 9 (22) (2021) 2855.
[57] C. Ramírez-Martínez, L.A. Zárate-Hernández, R.L. Camacho-Mendoza, S. González-Montiel, A. Meneses-Viveros, J. Cruz-Borbolla, The use of global and local reactivity descriptors of conceptual DFT to describe toxicity of benzoic acid derivatives, Comput. Theor. Chem. 1226 (2023) 114211.
[58] E.M. Collins, K. Raghavachari, Effective molecular descriptors for chemical accuracy at dft cost: fragmentation, error-cancellation, and machine learning, J. Chem. Theor. Comput. 16 (8) (2020) 4938–4950.
[59] R.O. Kareem, O.A. Hamad, H. Kebiroglu, B.A. Mohammed, Spectroscopic properties and computational studies of phosphosilicate-doped compounds including (F, Cl, Br), J. Chem. Lett. 5 (3) (2024) 159–167.
[60] T. Lu, F. Chen, Multiwfn: a multifunctional wave function analyzer, J. Comput. Chem. 33 (5) (2012) 580–592.
[61] W. Humphrey, A. Dalke, K. Schulten, VMD:visual molecular dynamics, J. Mol. Graph. 14 (1) (1996) 33–38.
[62] A.V. Shishkina, V.V. Zhurov, A.I. Stash, M.V. Vener, A.A. Pinkerton, V.G. Tsirelson, Noncovalent interactions in crystalline picolinic acid N-oxide: insights from experimental and theoretical charge density analysis, Cryst. Growth Des. 13 (2) (2013) 816–828.
[63] M. Bohlén, K.C. Satyanarayana, K. Bolton, Computational studies of poly (vinylidene fluoride) single wall carbon nanotube systems, J. Comput. Theor. Nanosci. 10 (6) (2013) 1317–1325.